Title

Iodide-doped precious metal nanoparticles: measuring oxidative stress in vivo via photoacoustic imaging

Journal

Nanoscale, 12(19)

ISSN

2040-3364

Authors

Mantri, Yash
Davidi, Barak
Lemaster, Jeanne E
et al.

Publication Date

2020-05-21

DOI

10.1039/d0nr03047c

Peer reviewed

HHS Public Access

Author manuscript

Nanoscale. Author manuscript; available in PMC 2021 May 21.

Published in final edited form as:

Nanoscale. 2020 May 21; 12(19): 10511–10520. doi:10.1039/d0nr03047c.

Iodide-doped Precious Metal Nanoparticles: Measuring Oxidative Stress *in vivo* via Photoacoustic Imaging

Yash Mantri[1], **Barak Davidi**[2], **Jeanne E. Lemaster**[3], **Ali Hariri**[3], **Jesse V. Jokerst**[*,3,4,5]

[1]Department of Bioengineering University of California, San Diego, La Jolla, CA, USA.

[2]Department of Physics, Fairfield University, Fairfield, CT, USA.

[3]Department of NanoEngineering, University of California, San Diego, La Jolla, CA, USA.

[4]Materials Science Program, University of California, San Diego, La Jolla, CA, USA.

[5]Department of Radiology, University of California, San Diego, La Jolla, CA, USA.

Abstract

Accumulation of reactive oxygen and nitrogen species (RONS) can induce cell damage and even cell death. RONS are short-lived species, which makes direct, precise, and real-time measurement difficult. Biologically-relevant RONS levels are in the nM-μM scale; hence, there is a need for highly sensitive RONS probes. We previously used hybrid gold-core silver-shell nanoparticles with mM sensitivity to H_2O_2. These particles reported the presence of RONS via spectral shifts which could easily be quantified via photoacoustic imaging. Here, we used halide doping to tune the electrochemical properties of these materials to better match the oxidation potential of RONS. This work describes the synthesis, characterization, and application of these AgI-coated gold nanorods (AgI/AuNR). The I:Ag molar ratio, pH, and initial Ag shell thickness were optimized for good RONS detection limits. Halide doping lowers the reduction potential of Ag from E^0_{Ag} = 0.80 V to E^0_{AgI} = − 0.15 V resulting in a 1000-fold increase in H_2O_2 and 100,000-fold increase in $ONOO^-$ sensitivity. The AgI/AuNR system also etches 45-times faster than undoped Ag/AuNR. The AgI/AuNR easily reported the endogenously produced RONS in established cells lines as well as murine models.

Graphical Abstract

*Corresponding Author: jjokerst@ucsd.edu.

Conflicts of Interest

There are no conflicts to declare.

Supporting Information

Additional ICP-MS measurements, DLS Absorption, Photostability, Photoacoustic, Kinetic, Fluorescence imaging, cell-culture, cytotoxicity, *in vivo* negative controls and PA spectral data.

Iodide-doping of silver coated gold nanorods increases sensitivity to RONS.

Keywords

Reactive oxygen and nitrogen species; photoacoustic imaging; optoacoustic imaging; halide doping; gold nanoparticles; silver nanoparticles; oxidative stress

Introduction.

Reactive oxygen and nitrogen species (RONS) are naturally produced byproducts of aerobic metabolism.[1, 2] Low levels of RONS play a regulatory role via autophagy and are also involved in cell signaling.[3, 4] Under oxidative stress conditions, RONS production increases dramatically leading to degradation of proteins, lipids, DNA, cell cycle arrest and even cell death.[4–6] Dysregulated RONS can lead to diseases such as cancer,[7–9] Alzheimer's disease,[10] and heart disease.[11] RONS are short-lived species, which makes direct, precise, and real-time measurements difficult. Quantitative analysis of these redox radicals is generally difficult due to high concentrations of glutathione, varying concentrations of metals, and other redox-sensitive agents, which can catalyze or inhibit radical reactions.[12, 13] Physiologically, RONS are found as a milieu of oxidative species which include radicals such as hydrogen peroxide, peroxynitrate, superoxide, hydroxyl, hypochlorite, nitroxyl, singlet oxygen, nitric oxide and many more.[14, 15] A mixture of these species causes more damage in comparison to one oxidant at high concentration.[14]

There are several existing approaches to measuring RONS. Fluorescent molecules such as 2',7' – dichlorofluorescin diacetate (DCFDA) offer *in vitro* assessments.[13, 16–18] Fluorescent probes provide high sensitivity and real time imaging but have limited utility *in vivo*. Electrochemical biosensors made from single walled carbon nanotubes have also shown nanomolar sensitivity to H_2O_2 in macrophage cells:[19] These are useful tools to study metabolic pathways in single cells but are difficult to implement in tissue systems. *In vivo* imaging of H_2O_2 in real time using a chemoselective bioluminescent reporter (peroxy-caged luciferin-1) has also been reported.[20] Unfortunately, this technique requires genetically modified cells that produce luciferase and therefore not viable for clinical applications. Furthermore, these purely optical methods are limited by poor penetration through tissue.

In contrast to optical methods, photoacoustic (PA) imaging is an excellent non-invasive tool that combines the depth penetration and high resolution of ultrasound with the high contrast and spectral capabilities of optical imaging.[21–23] Photoacoustic signal is generated when an absorbing particle undergoes thermoelastic expansion under pulsed illumination. Expansion

results in the formation of acoustic pressure waves that is detectable by ultrasound. Nanoparticles are often used as activatable, exogenous contrast agents in PA due to highly tunable shape, size and functionalization.[24–28] PA has been used to image RONS species previously using semiconductor polymer nanoparticles,[29, 30] but RONS imaging has not yet leveraged the incredibly high molar extinction coefficients of plasmonic particles[31, 32] for ultralow detection limits. Indeed, gold nanorods (AuNR) are often employed as PA contrast agents because of their high photothermal conversion efficiency and relative chemical inertness.[33–35] Tuning the aspect ratio of AuNR allows one to engineer particles that have a maximum absorbance within the biological optical window,[36–39] and AuNRs have been used with PA to sense chemical species, track cells, image tumors, and as theranostic tools.[33, 40–42]

Many PA probes take an “always on” approach via enhanced accumulation, permeability and retention effect to generate PA contrast in images. Other probes respond to biochemical cues via an activatable signal for both *in vitro* and *in vivo* applications.[27, 43–53] Previously, we and others have reported silver/gold theranostic nanoparticles for RONS sensing and antibacterial treatment.[33, 54] This was silver shell/gold core nanorods (Ag/AuNR) that selectively etched silver ions in the presence of RONS (H_2O_2 and $ONOO^-$) with reporting via PA imaging via spectral shifts. The bare AuNR have a near infrared (NIR) resonance that is blue-shifted after the shell is added. When the shell is oxidized by the RONS, the NIR resonance is restored and the resulting PA signal directly reports the quantity of RONS (Figure 1A). Thus, this PA signal reports the amount of Ag^+ released and the quantity of RONS. However, this system required mM concentrations of RONS to etch the silver coating and activate the system—this was a fundamental limitation of this work because biologically relevant concentrations are on the nM to μM scale.[55–59]

In this work, we used electrochemical principles and nanoengineering to make the nanoparticle sensitive to lower RONS concentrations. More specifically, we doped the silver shell with iodide because this doping would reduce the standard reduction potential of the silver to more closely match the oxidation potential of the RONS species. After careful characterization of the product, we validated this system in both *in vitro* and *in vivo* models of human disease. The iodide-doped system offers detection limits that are three to five log orders lower than un-doped systems and underscores the utility of this material for imaging RONS.

Rationale for Iodide Doping and Synthetic Control.

One possible way to increase sensitivity to RONS is to reduce the reduction potential of the Ag shell (E^0_{Ag} = 0.80 V) to better complement the reduction potentials of the RONS. Doping Ag with halides would lower the reduction potential (E^0_{AgF} = 0.78 V, E^0_{AgCl} = 0.22 V, E^0_{AgBr} = 0.07 V, and E^0_{AgI} = − 0.15 V). However, it is necessary to stabilize the shell because silver and silver halides are photosensitive making them unfavorable candidates for PA imaging.[60] Fortunately, the gold core offers abundant electrons to stabilize the Ag shell for halide doping.[61–63] We selected AgI because it is the least photosensitive and has the lowest standard reduction potential of the four halides. It resists reduction by metals but is etched under acidic conditions.[64] Doping halides into bulk Ag is diffusion limited.[63, 65–67]

The X^- is chemically adsorbed on the surface forming a porous film through which more X^- can diffuse through the bulk metal. Iodide is more aggressive in doping into Ag due to its higher polarizability, increased stability, lower reduction potential, and low activation energy versus other halides.[66] I^- also forms a more porous film than Cl^- and Br^- leading to higher dopant concentrations.[66–69]

Results and Discussion

Synthesis of Ag/AuNR.

Figure 1B–E shows TEM images and Figure 1G shows the absorption spectra of AuNRs and Ag/AuNRs with varying shell thickness. The AuNR had an aspect ratio of 3.1 ± 0.44 (n > 150 particles) with a peak absorbance at 735 nm. The color of the colloidal suspension changed from brown to green to purple to red and finally orange with increasing shell thickness (Figure 1F). The Ag:Au molar ratio increased linearly ($R^2 = 0.93$) with increasing amounts of added Ag (Figure S1). Increasing shell thickness results in a blue shift of the absorption spectrum due to reduction of the aspect ratio from 3.1 to 1.25 for 15 nm shells (Ag:Au = 3.71; Figure 1G). Increasing the amount of Ag results the emergence of a new 400 nm peak which can be attributed to the unsymmetrical growth of the silver shell.[33, 70, 71] This was further confirmed with dynamic light scattering (DLS) (Figure S2). DLS studies then hydrodynamic diameter of a particle, which is assumed to be spherical. This is a major limitation of this technique to characterize rod like structures. Here, two peaks are seen for all samples. The smaller peak (5–7 nm) is attributed to the rotational diffusion coefficient of non-spherical AuNRs.[72] After silver coating and subsequent iodide doping, the hydrodynamic diameter increases by 2.5 nm along with the rotational diffusion coefficient as particles increase in size.[70, 71]

There are three synthetic “knobs” to optimize the doping of the Ag shell: molar ratio of I:Ag, pH, and the initial Ag shell thickness (see Figure S3). The molar ratio of I:Ag had relatively minor effects. Excess iodide results in the leaching of Ag from the gold surface and the formation of Ag nanoparticles—this further increases the absorbance at 390 nm (Figure S3A). The peak broadening and baseline increase in absorbance at high I:Ag ratio suggests particle destabilization and aggregation. A 1:1 molar ratio of I:Ag showed no peak shift but produced the predicted dampening in absorbance indicating successful doping.[63, 73]

The pH is the most important variable in determining doping because iodide is best doped into Ag under acidic conditions.[67, 74] However, in excessively acidic media, Ag can be oxidized and etched off the gold core (Figure S3B). The red-shift, lower absorbance, and peak broadening seen at pH 2, 3, and 4 suggest Ag shell etching and Au core degradation. In more basic conditions, the forward reaction is unfavorable as shown in Equation 1. Hence, pH 5 was selected as the most favorable condition.

$$Ag_n + mH^+ + mI^- \rightarrow Ag_{n-m}(AgI)_m + (m/2)H_2 \quad \text{Equation 1}$$

The initial Ag shell thickness could also affect the final product because a thinner shell is more susceptible to changes in pH (Figure S3C). Aqueous suspensions of Ag/AuNRs with

varying shell thicknesses were adjusted to pH 5 and doped with a 1:1 ratio of I:Ag. The nanoparticles with thinner shells showed more peak broadening compared to their undoped controls. Iodide impurities in CTAB is known to disrupt AuNRs which reaffirms the importance of a thicker (> 4 nm) Ag protective shell.[75–77] Particles with a Ag:Au molar ratio of 3.32 or more (through ICP-MS) showed no change in their spectra and were further characterized and used for all other tests.

Characterization of iodide doping.

The electrons supplied by the gold core stabilizes and maintains the silver shell on the Au for successful I^- doping.[63] In this design, these electrons are from the Au core.[62] The initial I^- adsorption results in dampening of the 390 nm peak (Figure 2A and Figure S3A). The slight red shift of the transverse peak to 395 nm accompanied by peak broadening indicates the formation of bulk AgI.[67] However, there are many sources of spectral error, and thus we used complementary techniques to confirm these observations.

EDX spectroscopy was used to further characterize the particles (Figure 2B). Bare AuNR showed slight amounts of Ag because Ag is used to control the anisotropic growth of AuNRs during synthesis.[78, 79] I (0.2 wt%) was detected in bare AuNR possibly due to contamination in the CTAB used during synthesis.[77] However, the iodide contamination had no effect on rod formation with rod yield greater than 90%. The Ag/AuNRs showed clear peaks of Au and Ag with a Ag:Au molar ratio of 2.3 that was further confirmed by ICP – MS (Ag:Au = 3.32) (Figure S1). Iodide-doped Ag/AuNRs showed characteristic peaks for iodide with a I:Ag molar ratio of 0.5 (starting concentration was 1:1). While EDX is obviously a surface weighted technique, this EDX data suggests that not all of the I^- formed AgI, which is expected because doping initially starts with surface adsorption and complex formation followed by diffusion-mediated doping.[69]

The *p*XRD analysis of all samples showed characteristic peaks for Au and Ag (JCPDS 04–0784 and 04–0783) (Figure 2C). The crystal structure for Au and Ag are very similar, and it is difficult to separate one from the other. The formation of AgI is obvious on the *p*XRD analysis for AgI/AuNR (Figure 2C). The presence of characteristic α-AgI_3O_8 peaks representing the 111, 004, and 114 crystallographic planes (JCPDS 66–0314) further suggest that the adsorbed AgI is complexed with oxygen. Furthermore, the 100, 101, and 110 peaks for β-AgI (JCPDS 09–0374) show that bulk AgI also exists in the sample. The presence of crystalline β-AgI could also be attributed to AgI nanoparticle formation due to Ag leaching from the gold surface. TEM images of AgI/AuNRs showed the preservation of the shell-core structure and no signs of Ag nanoparticle formation (Figure 2E and F). There was no significant change in coated particle size. This suggests that the doping must have occurred on and in the shell with bulk AgI in the shell and AgI_3O_8 at the surface.

We also studied the surface chemistry using zeta potential (Figure 2G). The zeta potential of Ag/AuNRs becomes more positive with iodide doping. This is because the KI removes the NO_3^- counter ion from the Ag surface as KNO_3.[67] Preoxidation of the surface Ag atom by a nucleophile imparts a small positive charge at the surface and a corresponding negative charge within the particle.[67, 80] This high charge facilitates the high colloidal stability of AgI/AuNRs.

Finally, we studied the photostability of AgI/AuNRs over 5 minutes of 680 nm pulsed laser illumination (Figure S4). the PA intensity reduced only 17% over 5 minutes indicating that synthesized AgI/AuNR are stable under pulsed laser illumination.

In vitro RONS sensing.

Figure 3 shows the iodide-doped particles' response to RONS. TEM images (Figure 3A–F) pre-and-post etching with 0.5 mM H_2O_2 showed that H_2O_2 had no effect on AuNR, slight etching on Ag/AuNRs, and complete shell removal for AgI/AuNRs. The H_2O_2 treatment causes selective AgI shell etching and the recovery of core AuNR's original spectrum (Figure 3G). The detection limit for H_2O_2 and $ONOO^-$ with the iodide-doped particles are 50 μM and 100 nM respectively, which is 1000-fold and 100,000-fold more sensitive than undoped Ag/AuNR controls (Figure 3 I–J) ($p < 0.05$, n=3). Increased sensitivity to H_2O_2 ($E^0_{H2O2} = 0.87$ V in alkaline conditions) and $ONOO^-$ ($E^0_{ONOO-} = 1.2$ V) due to iodide-doping can be credited to the lower standard reduction potential of AgI ($E^0_{AgI} = -0.15$ V) and ($E^0_{AgIO3} = 0.35$ V) compared to Ag ($E^0_{Ag} = 0.80$ V). The higher sensitivity to $ONOO^-$ is likely due to its higher reduction potential. The undoped Ag/AuNR are responsive to 50 mM H_2O_2 and 1 mM $ONOO^-$. It is also possible that AgI_3O_8/AgI layers in the iodide-doped samples become oxidized and then etch off more readily compared to the undoped controls. Our previous work showed that Ag/AuNR were responsive to 5 mM H_2O_2 and 0.25 mM $ONOO^-$, which is lower than this study. The difference in RONS response can be attributed to batch-to-batch variability of particles and to different shell thicknesses. Our previous work used thicker shelled particles.

We also tested the response of AgI/AuNR to 1 mM of other redox species (Figure 3K). Etching selectivity is a function of the reduction potential of the oxidative species (Figure 3H). Reduction potential is the tendency of a chemical species to gain or lose electrons. A more positive redox potential implies a greater tendency to gain electrons and become reduced. As a result, $^{\bullet}OH$ ($E^0_{^{\bullet}OH} = 2.8$ V) had the most effect, and O_2^- ($E^0_{O2-} = -2.4$ V) had the least effect on the particles. The variation in etching is understandable as high positive reduction potential of $^{\bullet}OH$ makes it a good electron acceptor whereas a negative reduction potential for O_2^- makes it a great electron donor. The slight negative reduction potential of AgI makes it a good electron donor to $^{\bullet}OH$ and in turn get oxidized off the Au core. The high oxidizing power of $^{\bullet}OH$ etches off the AgI shell and further degrades the Au core ($E^0_{Au} = 1.69$ V) as observed in the absorption spectrum (Figure 3K).

Kinetically, AgI/AuNR etches ~45 times faster than Ag/AuNR when treated with 50 mM H_2O_2 (Figure S7B). The detection limit of $ONOO^-$ and H_2O_2 with photoacoustic imaging followed the same trend as the absorbance (Figure 4 B–C and Figure S6). A significant increase ($p < 0.001$) in photoacoustic signal is observed versus baseline with 10^{-5} mM of $ONOO^-$ and 10^{-2} mM of H_2O_2. AuNR treated with 10 mM H_2O_2 showed an uncharacteristic PA enhancement. H_2O_2 is known to decompose under high fluence illumination into water and oxygen. At high enough concentrations of 10 mM there could be oxygen nanobubble formation and PA enhancement due to cavitation. In addition, plasmonic materials are known to aggregate at higher ionic strength.

While these initial experiments tested individual RONS species, the *in vivo* situation is a complex milieu of RONS. Thus, we used SKOV3 cells to model this milieu because they are known to produce high levels of free radicals.[33, 81–83] The DCFDA assay (Figure S8) confirmed that SKOV3 cells endogenously produce RONS, and that these RONS are scavenged with NAC. The nanoparticles were treated with cell-free media, SKOV3 media, and SKOV3 media treated with NAC (Figure S9). Photoacoustic signal from both Ag/AuNR and AgI/AuNR turned "ON" when treated with RONS-enriched media.

The MTT assay for cell cytotoxicity (Figure S10) showed that nanoparticles at 0.01–0.1 nM had no toxicity versus the PBS negative control. At high concentrations of 1 nM, particles exhibited higher toxicity which can be attributed to the higher amounts of residual CTAB in those samples. Hence, all *in vivo* experiments were carried out at 0.3 nM particle concentrations to keep toxicity as low as possible and generate sufficient signal from the nanoparticles.

In vivo RONS sensing.

Finally, we used zymosan to stimulate intramuscular RONS generation in a murine model (n=3). Figure 5 shows the response of AuNR, Ag/AuNR, and AgI/AuNR to endogenously-generated RONS. Over 90 minutes, the photoacoustic signal from AgI/AuNR in the presence of RONS increased by 70% compared to 20% for Ag/AuNR. The AuNR signal reduced by 10% which can be attributed to laser-induced nanorod deformation.[84, 85] Photoacoustic spectral data showed a clear increase in photoacoustic intensity at 680 nm for AgI/AuNR and no change for Ag/AuNR and AuNR. AgI/AuNR turned on only in the presence of RONS as zymosan-free controls showed < 5% change in signal over 90 minutes (Figure S11).

Conclusion.

This work presents the synthesis, characterization and application of a hybrid iodide-doped Au/Ag nanoparticle. In summary, iodide can be doped into Ag/AuNR under acidic conditions. The I:Ag molar ratio and initial thickness of Ag shell play an important role in successful iodide doping, which lowers the reduction potential of the Ag shell making the nanoparticles 1,000 times more sensitive to H_2O_2 and 100,000 times more sensitive to $ONOO^-$ compared to undoped Ag/AuNR. Photoacoustic imaging can be used to sense RONS levels *in vivo*. Importantly, the Ag^+ and I^- released here can also serve as antibacterial agents, and future work will test the antibacterial efficacy of these materials including in smart wound dressings.

Materials and Methods

Materials.

Hexadecyltrimethylammonium bromide (CTAB, Cat. #1102974), gold (III) chloride trihydrate (Cat. #520918), L-ascorbic acid (Cat. #A7506), silver nitrate (Cat. #209139), sodium borohydride (Cat. #2133462), potassium iodide (Cat. #746428), sodium hydroxide (Cat. #S5881), hydrochloric acid (Cat. #339253), hydrogen peroxide (Cat. #216763), potassium superoxide (Cat. #278904), sodium hypochlorite (Cat. #239305), tert-butyl

hydroperoxide (Cat. #416665), tert-butyl peroxide (Cat. #168521), sodium nitrite (Cat. #237213), Angeli's salt (Cat. #176695), iron (II) perchlorate hydrate (Cat. #33408), 2',7'-dichlorofluorescin diacetate (DCFDA Cat. #D6883), N-acetylcysteine (NAC) from Escherichia coli (Cat. #A9165), and zymosan A from Saccharomyces cerevisiae (Cat. #Z4250) were purchased from Sigma-Aldrich (Atlanta, GA, USA). Peroxynitrite was purchased from EMD Millipore Co. (Cat. #516620, MA, USA). McCoy's 5A medium with L-glutamine, sodium bicarbonate; without phenol red was purchased from GE Healthcare Bio-Sciences Corp. (Cat. #SH30270.01, MA, USA). Vybrant MTT cell proliferation assay kit was purchased from Life Technologies Corp. (Cat. #V13154, NY, USA). All reagents were used without further purification. Aqueous solutions were made by diluting in distilled water unless otherwise mentioned.

Gold nanorod (AuNR) synthesis.

AuNRs were synthesized using the seed-mediated growth method used in a previous report with some modifications.[33] Gold seeds were prepared by adding 5 ml of CTAB (0.2 M) to 2.5 ml of $HAuCl_4.3H_2O$ (0.001 M) and further reduced with 0.6 ml of ice-cold $NaBH_4$ (0.01 M) under vigorous stirring for 2 min. The growth solution was prepared by adding 500 ml of $HAuCl_4●3H_2O$ (0.001 M) to 500 ml of CTAB (0.2 M). To this, 36 ml of $AgNO_3$ (0.004 M) and 7 ml of L-ascorbic acid (0.089 M) was added. Next, 1.2 ml of freshly prepared gold seed solution was added, and the reaction mixture was left undisturbed for 30 – 60 mins until the solution turned purple/dark brown. After 12 hrs of additional reaction the mixture was washed three times via centrifugation at 12500 rpm for 15 min with distilled water to remove excess CTAB and unreacted gold. Synthesized AuNR were suspended in distilled water and stored at 4 °C.

Preparation of the Silver-coated AuNR (Ag/AuNR) and Iodide-Doped AuNR (AgI/AuNRs).

Ag-coated AuNRs were synthesized using previous reports with a few modifications.[33, 71] Ag/AuNRs with increasing Ag-shell thickness were made by increasing the Ag:Au molar ratio: 80 μL of AuNR stock (AuNR concentration 10.95 nM) was suspended in a mixture containing 1.5 ml distilled water and 1 ml CTAB (0.1 M). Next, various amounts of $AgNO_3$ (0.01 M) 25, 45, 65, 85, 110, 145, and 175μL were added to separate vials and stirred at 600 rpm. Then, 110 μL of L-ascorbic acid (0.1 M) and 300 μL of NaOH (0.1 M) was added under vigorous stirring for 30 min. The synthesized Ag/AuNR shell/core particles were washed twice via centrifugation at 12500 rpm for 15 min to remove excess Ag and CTAB. Iodide doping of Ag to form AgI can be done under acidic conditions as proposed by Mulvaney and later demonstrated by Vasan.[67, 74] We studied the effect of Ag:I molar ratio, pH, and initial Ag shell thickness on iodide doping. Finally, Ag/AuNR with a Ag:Au molar ratio of 3.32 were doped with iodide by first adjusting pH to 5 using HCl (0.1 M) and adding KI in a 1:1 molar ratio of Ag:I. The reaction was stirred at 600 rpm for 2 hours to ensure complete doping. The doped particles were washed twice with centrifugation at 12500 rpm for 15 min to remove unreacted iodide. The particles were stored at 4°C wrapped in aluminum foil to prevent any photoetching.

Transmission Electron Microscopy (TEM).

TEM samples were examined using a JEOL JEM-1400Plus transmission electron microscope operating at 80 kV. Images were recorded using a Gatan OneView 4K digital camera and processed using ImageJ 1.51s. Samples were prepared by drop casting 20 μL of nanoparticle suspension onto 300 mesh carbon-coated copper grids.

Absorption spectra.

All absorption spectra were measured using a Molecular Devices Spectramax M5 microplate reader using 150 μL of solution in 96-well plates. Unless otherwise mentioned, absorbance was read from 350 – 900 nm with a step size of 10 nm and plotted using GraphPad Prism Software.

Energy Dispersive X-Ray Spectroscopy (EDX).

EDX samples were analyzed using FEI Apreo FESEM, operating at 20 kV with a spot size of 5 and emission current −90 μA; 20 μL of sample were drop-cast onto 300-mesh carbon-coated copper grids.

Powder X-Ray Diffraction (pXRD).

Samples were characterized by pXRD with the Bruker D8 Advance used in Bragg-Brentanno geometry. Cu radiation: 1.54 Angstroms, equipped with a Ni K-beta filter. The 2θ scan range was 10–80^{o} in increments of 0.02 and exposure of 0.25 seconds per scan. Samples were prepared by spinning down 1000 μL of nanoparticle suspension and resuspending them in 20 μL of water via sonication.

Dynamic light scattering (DLS) and zeta potential.

Hydrodynamic diameter and zeta potential were measured using a Malvern Instruments Zetasizer ZS 90; 200 μL of nanoparticle suspension was diluted in 800 mL of distilled water.

Inductively Coupled Plasma - Mass Spectrometry (ICP-MS).

The ICP-MS analysis was done on a Thermo Scientific iCAP RQ ICP-MS in the Environmental and Complex Analysis Laboratory at UC San Diego. Samples were washed twice to remove unreacted reagents and then digested overnight in *aqua regia* before analysis.

RONS selectivity and sensitivity studies.

To compare the dose dependent response of the particles, 200 μL of AuNR, Ag/AuNR and AgI/AuNR were treated with 10^{-3}, 5^{-3}, 10^{-2}, 5^{-2}, 10^{-1}, 5^{-1}, 1, 5, 10, and 50 mM of H_2O_2 for 18 hours at room temperature. Separately, particles were also treated with 10^{-6}, 10^{-5}, 10^{-4}, 10^{-3}, 10^{-2}, 10^{-1}, 1, and 10 mM of $ONOO^-$ for 18 hours at room temperature. Absorption spectra after treatment with H_2O_2 and $ONOO^-$ was taken and plotted ratiometrically as Absorbance at 780 nm:Absorbance at 578 nm. The rationale behind the choice of wavelength; 780 nm is the peak absorbance of the etched-AgI/AuNR treated with 50 mM H_2O_2 and 578 nm is the peak absorbance of unetched AgI/AuNR.

To test RONS selectivity, nanoparticles were treated with 1 mM of hydrogen peroxide (H_2O_2), peroxynitrite ($ONOO^-$), nitroxyl (HNO), nitrite (NO_2^-), tert-butoxy radical ($C_4H_9O^\bullet$), tert-butyl hydrogen peroxide (tBuOOH), hypochlorite (OCl^-), superoxide (O_2^-), and hydroxyl radical ($^\bullet OH$). Hydroxyl radicals were generated via the Fenton Reaction between H_2O_2 and iron (II) perchlorate hydrate ($Fe(ClO_4)_2 \bullet xH_2O$).[59]

Etching Kinetics.

The kinetics of Ag and AgI etching were studied using change in absorbance at 680 nm when treated with 0.5 and 50 mM H_2O_2 over 18 hours at room temperature with a step size of 10 min.

Cell culture.

To test whether endogenously produced RONS can oxidize the Ag and AgI shell, we treated AuNR, Ag/AuNR, and AgI/AuNR with cell media from ovarian cancer cell cultures (SKOV3). The 2'−7' dichlorofluorescin diacetate (DCFDA) assay was used to confirm that SKOV3 cells naturally produce RONS. Briefly, cells were cultured using phenol free McCoy's 5A medium; 10,000 cells were plated onto 12-well tissue culture plates and incubated till 80% confluent. Cells were incubated with DCFDA (20 μM in PBS) for 45 minutes in the dark and imaged using a Life Technologies EVOS FL microscope with FITC filter sets at 10X magnification. As a negative control, cells were treated with N-acetyl cysteine (NAC; final concentration 10 mM in PBS) for 1 hour to scavenge RONS. Finally, 200 μL of nanoparticle suspension was treated with 200 μL of SKOV3 cell media and incubated for 30 min. Photoacoustic response was studied at 680 nm. Nanoparticle cytotoxicity was assessed using the MTT cell proliferation assay kit.

Photoacoustic imaging.

All photoacoustic images were acquired using the Visualsonics Vevo 2100 LAZR imaging system at 680 nm. All photoacoustic spectra were acquired from 680 – 970 nm with a step size of 5 nm. All *in vitro* samples were imaged using the LZ250 transducer (21 MHz center frequency) and all *in vivo* studies were imaged using the LZ550 transducer (40 MHz center frequency).

In Vivo RONS sensing.

All animal experiments were performed in accordance with NIH guidelines approved by the Institutional Animal Care and Use Committee (IACUC) under protocol S15050 at the University of California, San Diego. Zymosan was used to stimulate endogenous production of RONS in a murine model.[30, 59, 86] 100 μL of zymosan (20 mg/ml in PBS) was injected intramuscularly into the femoris muscle of the upper hind limb and incubated for 20 min ($n = 3$). After incubation 100 μL of AuNR, Ag/AuNR and AgI/AuNR (0.3 nM particle concentration) was injected and their photoacoustic response was monitored at 0, 5, 10, 15, 20, 30, 45, 60 and 90 minutes. We used zymosan only and PBS injections as negative controls. All images were processed using the Vevo LAB 3.1.0 software. We studied the increase in photoacoustic response as a ratio of photoacoustic intensity at t = x minutes:photoacoustic intensity at t = 0 min.

Supplementary Material

Refer to Web version on PubMed Central for supplementary material.

Acknowledgments

Figure 1A and table of contents figure was created with BioRender.com. J.E.L. acknowledges funding from the National Institutes of Health (NIH) Institutional National Research Service Award T32 CA153915, Cancer Researchers in Nanotechnology (Zhang). J.V.J. acknowledges funding from the NIH (DP2 HL137187) and infrastructure from S10 OD021821 and S10 OD023555. The transmission electron micrographs were taken in the Cellular and Molecular Medicine Electron microscopy core facility which is supported in part by National Institutes of Health Award number S10 OD023527. This work was performed, in part, at the San Diego Nanotechnology Infrastructure of UCSD, a member of the National Nanotechnology Coordinated Infrastructure, which is supported by the National Science Foundation (Grant ECCS-1542148). The authors also appreciate funding from the University of California Cancer Research Coordinating Committee (CRN-19-582184). B.D. acknowledges funding from NSF EEC-1852609.

References

1. Apel K and Hirt H, Annu Rev Plant Biol, 2004, 55, 373–399. [PubMed: 15377225]
2. Murphy MP, Biochemical journal, 2009, 417, 1–13. [PubMed: 19061483]
3. Schieber M and Chandel NS, Current biology, 2014, 24, R453–R462. [PubMed: 24845678]
4. Scherz-Shouval R and Elazar Z, Trends in cell biology, 2007, 17, 422–427. [PubMed: 17804237]
5. Boonstra J and Post JA, Gene, 2004, 337, 1–13. [PubMed: 15276197]
6. Fleury C, Mignotte B and Vayssière J-L, Biochimie, 2002, 84, 131–141. [PubMed: 12022944]
7. Nathan C and Cunningham-Bussel A, Nature Reviews Immunology, 2013, 13, 349.
8. Carden DL and Granger DN, The Journal of pathology, 2000, 190, 255–266. [PubMed: 10685060]
9. Medzhitov R, Nature, 2008, 454, 428. [PubMed: 18650913]
10. Pedersen JT, Chen SW, Borg CB, Ness S, Bahl JM, Heegaard NH, Dobson CM, Hemmingsen L, Cremades N and Teilum K, Journal of the American Chemical Society, 2016, 138, 3966–3969. [PubMed: 26967463]
11. Sverdlov AL, Elezaby A, Qin F, Behring JB, Luptak I, Calamaras TD, Siwik DA, Miller EJ, Liesa M and Shirihai OS, Journal of the American Heart Association, 2016, 5, e002555. [PubMed: 26755553]
12. Mailloux RJ, McBride SL and Harper M-E, Trends in biochemical sciences, 2013, 38, 592–602. [PubMed: 24120033]
13. Degli Esposti M, Methods, 2002, 26, 335–340. [PubMed: 12054924]
14. Weidinger A and Kozlov AV, Biomolecules, 2015, 5, 472–484. [PubMed: 25884116]
15. Bhattacharyya A, Chattopadhyay R, Mitra S and Crowe SE, Physiological reviews, 2014, 94, 329–354. [PubMed: 24692350]
16. Merksamer PI, Trusina A and Papa FR, Cell, 2008, 135, 933–947. [PubMed: 19026441]
17. Tanaka K, Miura T, Umezawa N, Urano Y, Kikuchi K, Higuchi T and Nagano T, Journal of the American Chemical Society, 2001, 123, 2530–2536. [PubMed: 11456921]
18. Gomes A, Fernandes E and Lima JL, Journal of biochemical and biophysical methods, 2005, 65, 45–80. [PubMed: 16297980]
19. Hicks J, Halkerston R, Silman N, Jackson S, Aylott J and Rawson F, Biosensors and Bioelectronics, 2019, 111430. [PubMed: 31299629]
20. Van de Bittner GC, Dubikovskaya EA, Bertozzi CR and Chang CJ, Proceedings of the National Academy of Sciences, 2010, 107, 21316–21321.
21. Xu M and Wang LV, Review of scientific instruments, 2006, 77, 041101.
22. Taruttis A and Ntziachristos V, Nature photonics, 2015, 9, 219.
23. Razansky D, Vinegoni C and Ntziachristos V, Optics letters, 2007, 32, 2891–2893. [PubMed: 17909608]

24. Fu T, Chen Y, Hao J, Wang X, Liu G, Li Y, Liu Z and Cheng L, Nanoscale, 2015, 7, 20757–20768. [PubMed: 26603315]
25. Chen F, Zhao ER, Hu T, Shi Y, Sirbuly DJ and Jokerst JV, Nanoscale Advances, 2019.
26. Moore C, Chen F, Wang J and Jokerst JV, Advanced drug delivery reviews, 2019.
27. Miao Q and Pu K, Bioconjugate chemistry, 2016, 27, 2808–2823. [PubMed: 27998078]
28. Yang X, Stein EW, Ashkenazi S and Wang LV, Wiley interdisciplinary reviews: nanomedicine and nanobiotechnology, 2009, 1, 360–368. [PubMed: 20049803]
29. Yang Z, Dai Y, Yin C, Fan Q, Zhang W, Song J, Yu G, Tang W, Fan W and Yung BC, Advanced Materials, 2018, 30, 1707509.
30. Pu K, Shuhendler AJ, Jokerst JV, Mei J, Gambhir SS, Bao Z and Rao J, Nature nanotechnology, 2014, 9, 233.
31. Chen Y-S, Zhao Y, Yoon SJ, Gambhir SS and Emelianov S, Nature nanotechnology, 2019, 14, 465.
32. Dreaden EC, Alkilany AM, Huang X, Murphy CJ and El-Sayed MA, Chemical Society Reviews, 2012, 41, 2740–2779. [PubMed: 22109657]
33. Kim T, Zhang Q, Li J, Zhang L and Jokerst JV, ACS nano, 2018, 12, 5615–5625. [PubMed: 29746090]
34. Jokerst JV, Cole AJ, Van de Sompel D and Gambhir SS, ACS nano, 2012, 6, 10366–10377. [PubMed: 23101432]
35. Tian L, Chen E, Gandra N, Abbas A and Singamaneni S, Langmuir, 2012, 28, 17435–17442. [PubMed: 23163716]
36. Kim F, Song JH and Yang P, Journal of the American Chemical Society, 2002, 124, 14316–14317. [PubMed: 12452700]
37. Gou L and Murphy CJ, Chemistry of materials, 2005, 17, 3668–3672.
38. Murphy CJ and Jana NR, Advanced Materials, 2002, 14, 80–82.
39. Gandra N and Singamaneni S, Advanced Materials, 2013, 25, 1022–1027. [PubMed: 23161698]
40. Jokerst JV, Thangaraj M, Kempen PJ, Sinclair R and Gambhir SS, ACS nano, 2012, 6, 5920–5930. [PubMed: 22681633]
41. Zhang Z, Wang J and Chen C, Theranostics, 2013, 3, 223. [PubMed: 23471510]
42. Yilmaz H, Bae SH, Cao S, Wang Z, Raman B and Singamaneni S, ACS Applied Nano Materials, 2019.
43. Levi J, Kothapalli SR, Ma T-J, Hartman K, Khuri-Yakub BT and Gambhir SS, Journal of the American Chemical Society, 2010, 132, 11264–11269. [PubMed: 20698693]
44. Wang S, Sheng Z, Yang Z, Hu D, Long X, Feng G, Liu Y, Yuan Z, Zhang J and Zheng H, Angewandte Chemie (International ed. in English), 2019, 58, 12415–12419. [PubMed: 31309679]
45. Yang Z, Song J, Tang W, Fan W, Dai Y, Shen Z, Lin L, Cheng S, Liu Y and Niu G, Theranostics, 2019, 9, 526. [PubMed: 30809290]
46. Weber J, Bollepalli L, Belenguer AM, Di Antonio M, De Mitri N, Joseph J, Balasubramanian S, Hunter CA and Bohndiek SE, Cancer research, 2019, 79, 5407–5417. [PubMed: 31455691]
47. Lu X, Zhao M, Chen P, Fan Q, Wang W and Huang W, Journal of Materials Chemistry B, 2018, 6, 4531–4538. [PubMed: 32254670]
48. Reinhardt CJ, Zhou EY, Jorgensen MD, Partipilo G and Chan J, Journal of the American Chemical Society, 2018, 140, 1011–1018. [PubMed: 29313677]
49. Wang S, Li Z, Liu Y, Feng G, Zheng J, Yuan Z and Zhang X, Sensors and Actuators B: Chemical, 2018, 267, 403–411.
50. Reinhardt CJ, Xu R and Chan J, Chemical Science, 2020.
51. Zhang J, Zhen X, Zeng J and Pu K, Analytical chemistry, 2018, 90, 9301–9307. [PubMed: 29940731]
52. Xie C, Zhen X, Lyu Y and Pu K, Advanced Materials, 2017, 29, 1703693.
53. Zhang J, Zhen X, Upputuri PK, Pramanik M, Chen P and Pu K, Advanced Materials, 2017, 29, 1604764.
54. Zhang Q, Cobley CM, Zeng J, Wen L-P, Chen J and Xia Y, The Journal of Physical Chemistry C, 2010, 114, 6396–6400.

55. Varma SD and Devamanoharan P, Free radical research communications, 1990, 8, 73–78. [PubMed: 2318421]
56. Varma S and Devamanoharan P, Free radical research communications, 1991, 14, 125–131. [PubMed: 2060858]
57. Giblin FJ, McCready JP, Kodama T and Reddy VN, Experimental eye research, 1984, 38, 87–93. [PubMed: 6705847]
58. Liu P, Xu B, Quilley J and Wong PY-K, American Journal of Physiology-Cell Physiology, 2000, 279, C1970–C1977. [PubMed: 11078713]
59. Hariri A, Zhao E, Jeevarathinam AS, Lemaster J, Zhang J and Jokerst JV, Scientific reports, 2019, 9, 1–10. [PubMed: 30626917]
60. Tan YT, MRS Bulletin, 1989, 14, 13–16.
61. Shankar C, Dao AT, Singh P, Higashimine K, Mott DM and Maenosono S, Nanotechnology, 2012, 23, 245704. [PubMed: 22641370]
62. Mott DM, Anh DTN, Singh P, Shankar C and Maenosono S, Advances in colloid and interface science, 2012, 185, 14–33. [PubMed: 22999044]
63. Linnert T, Mulvaney P and Henglein A, The Journal of Physical Chemistry, 1993, 97, 679–682.
64. Cappel CR, Kirk-Othmer Encyclopedia of Chemical Technology, 2000.
65. Singh P, Thuy NT, Aoki Y, Mott D and Maenosono S, Journal of Applied Physics, 2011, 109, 094301.
66. Ibrahim H, Mohammed S and Amin A, Int. J. Electrochem. Sci, 2010, 5, 278–294.
67. Ghosh S, Saraswathi A, Indi S, Hoti S and Vasan H, Langmuir, 2012, 28, 8550–8561. [PubMed: 22582868]
68. Kato Y, Ono LK, Lee MV, Wang S, Raga SR and Qi Y, Advanced Materials Interfaces, 2015, 2, 1500195.
69. Pedersen DB, Wang S, Duncan ES and Liang SH, The Journal of Physical Chemistry C, 2007, 111, 13665–13672.
70. Xiang Y, Wu X, Liu D, Li Z, Chu W, Feng L, Zhang K, Zhou W and Xie S, Langmuir, 2008, 24, 3465–3470. [PubMed: 18294010]
71. Liu M and Guyot-Sionnest P, The Journal of Physical Chemistry B, 2004, 108, 5882–5888.
72. Liu H, Pierre-Pierre N and Huo Q, Gold bulletin, 2012, 45, 187–195.
73. Gonzalez A, Noguez C, Ortiz G and Rodriguez-Gattorno G, The Journal of Physical Chemistry B, 2005, 109, 17512–17517. [PubMed: 16853239]
74. Mulvaney P, Langmuir, 1996, 12, 788–800.
75. Grzelczak M, Sánchez-Iglesias A, Rodríguez-González B, Alvarez-Puebla R, Pérez-Juste J and Liz-Marzán LM, Advanced Functional Materials, 2008, 18, 3780–3786.
76. Millstone JE, Wei W, Jones MR, Yoo H and Mirkin CA, Nano letters, 2008, 8, 2526–2529. [PubMed: 18642955]
77. Smith DK, Miller NR and Korgel BA, Langmuir, 2009, 25, 9518–9524. [PubMed: 19413325]
78. Walsh MJ, Barrow SJ, Tong W, Funston AM and Etheridge J, ACS nano, 2015, 9, 715–724. [PubMed: 25572634]
79. Grzelczak M, Pérez-Juste J, Rodríguez-González B and Liz-Marzán LM, Journal of Materials Chemistry, 2006, 16, 3946–3951.
80. Zhang A, Tie X, Zhang J, An Y and Li L, Applied Surface Science, 2008, 255, 3184–3187.
81. Saunders JA, Rogers LC, Klomsiri C, Poole LB and Daniel LW, Free Radical Biology and Medicine, 2010, 49, 2058–2067. [PubMed: 20934509]
82. Hileman EO, Liu J, Albitar M, Keating MJ and Huang P, Cancer chemotherapy and pharmacology, 2004, 53, 209–219. [PubMed: 14610616]
83. Fahrenholtz CD, Swanner J, Ramirez-Perez M and Singh RN, Journal of nanomaterials, 2017, 2017.
84. Link S, Burda C, Nikoobakht B and El-Sayed MA, The Journal of Physical Chemistry B, 2000, 104, 6152–6163.

85. Chen Y-S, Frey W, Kim S, Homan K, Kruizinga P, Sokolov K and Emelianov S, Optics express, 2010, 18, 8867–8878. [PubMed: 20588732]

86. Xie K, Yu Y, Zhang Z, Liu W, Pei Y, Xiong L, Hou L and Wang G, Shock, 2010, 34, 495–501. [PubMed: 20351628]

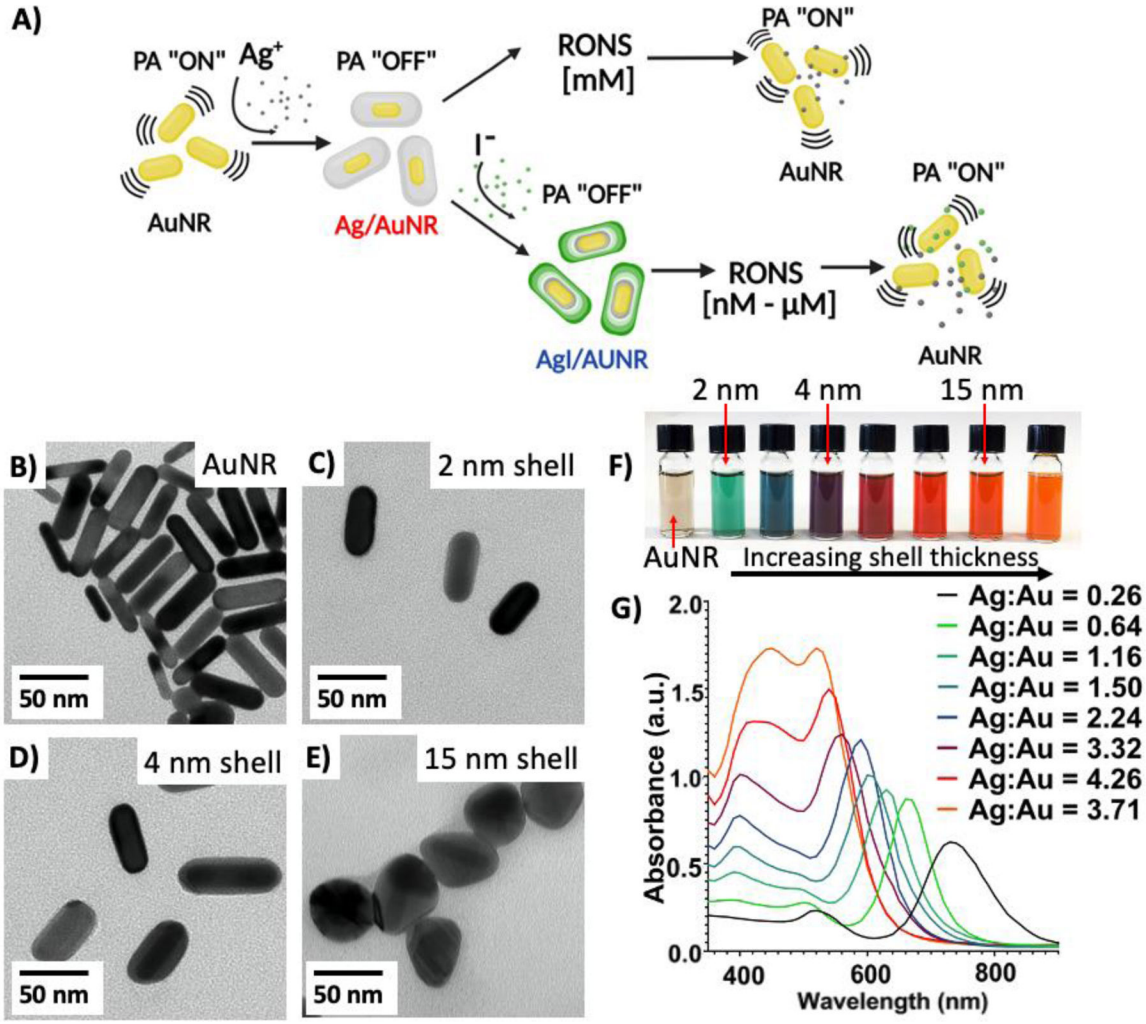

Figure 1. Schematic of shell optimization.

Schematic representation of the current work. Iodide doping results in biologically-relevant [nM - µM] sensitivity to RONS (**A**). TEM images of synthesized AuNR (**B**), Ag-coated AuNR with shell thickness 2 nm (**C**), 4 nm (**D**), 15 nm (**E**). Photograph of AuNR and Ag/AuNR with increasing shell thickness (**F**). The color changes from brown-green-purple-red-orange. Absorption spectra of AuNR and Ag/AuNR with increasing shell thickness (**G**). Increasing shell thickness results in a blue shift of the longitudinal plasmon peak as the aspect ratio reduces. Inset, final molar ratio of immobilized Ag:Au after coating through ICP-MS.

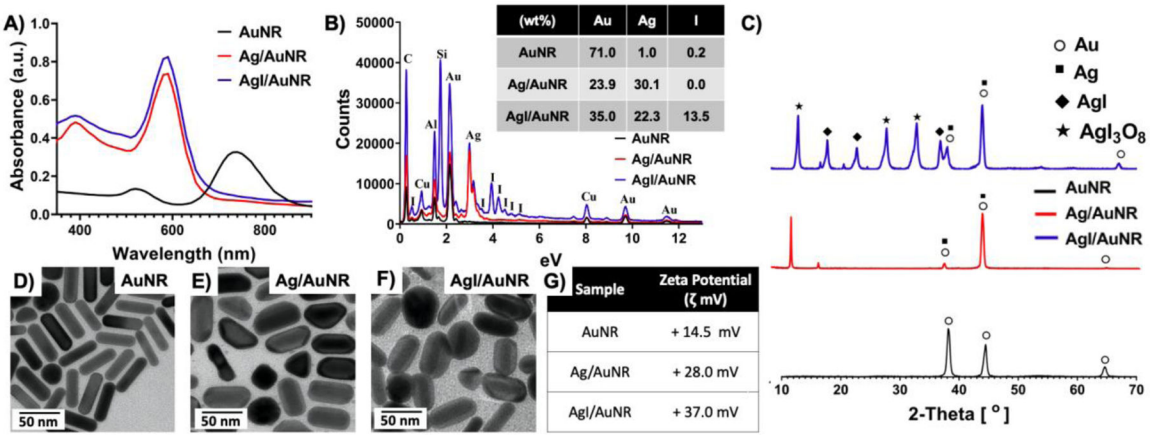

Figure 2. Characterization of iodide-doped Au/Ag hybrid nanoparticles.

(**A**) Absorption spectra of bare AuNR, Ag/AuNR, and iodide-doped Ag/AuNR (all samples were from the same batch of synthesis and doping). There is no change in the absorption spectra of doped and undoped Ag/AuNRs. EDX spectra (**B**) and *p*XRD analysis (**C**) of iodide-doped Ag/AuNRs show characteristic I^-, AgI, and AgI_3O_8 peaks. TEM images of AuNR (**D**), Ag/AuNR (**E**), and AgI/AuNR (**F**) show retention of the core-shell structure after iodide doping. There was no significant change in shell thickness on iodide doping. Doping iodine displaces the counter NO_3^- from the particle surface resulting in an increase in positive zeta potential (**G**).

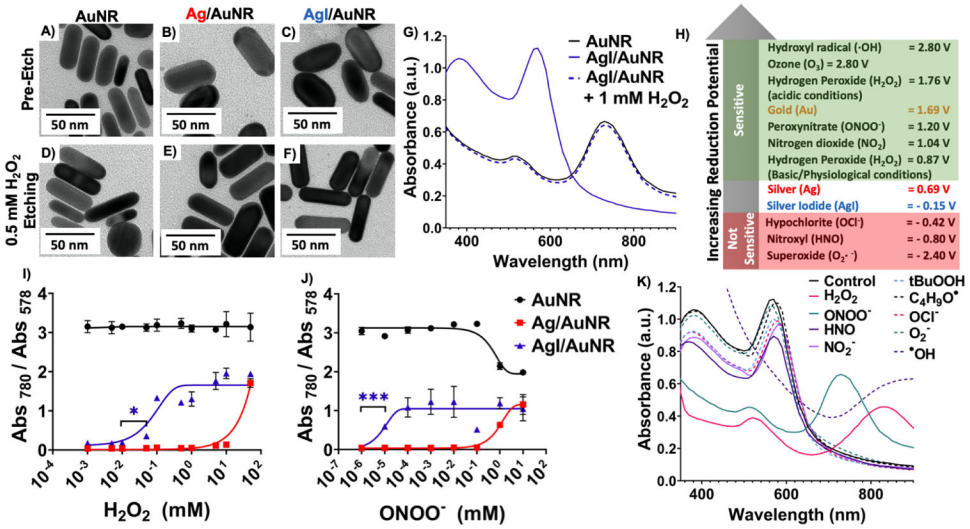

Figure 3. RONS sensitivity and selectivity.

TEM Images of AuNR, Ag/AuNR, and AgI/AuNR pre-and-post etching with 0.5 mM H_2O_2 (**A-F**). AgI/AuNR shows complete etching of AgI shell (**C, F**), AuNR and Ag/AuNR remain unaffected by H_2O_2. Bare AuNR has peak absorbance at 735 nm which blue-shifts on AgI coating. Subsequent etching with 1 mM H_2O_2 recovers the AuNR absorption spectrum (**G**). A slight negative reduction potential of AgI makes it a better electron donor and get oxidized by redox species with reduction potential higher than $E^0_{AgI} = -0.15$ V. Redox species with lower reduction potential cannot etch off the AgI shell (**H**). AgI/AuNR is 1000-fold more sensitive to H_2O_2 and 100,000-fold more sensitive to $ONOO^-$ compared to un-doped Ag/AuNR (**I-J**) (*n = 3*). RONS with positive reduction potential like H_2O_2 ($E^0_{H2O2} = 0.87$ V in alkaline/physiological conditions), $ONOO^-$ ($E^0_{ONOO-} = 1.2$ V), and $^{\bullet}OH$ ($E^0_{\bullet OH} = 2.8$ V) cause AgI shell etching whereas O_2^- ($E^0_{O2-} = -2.4$ V) had the least effect on the nanoparticles (**K**). Error bars represent the standard deviation of three replicate samples. *: $p<0.05$; **: $p<0.01$.

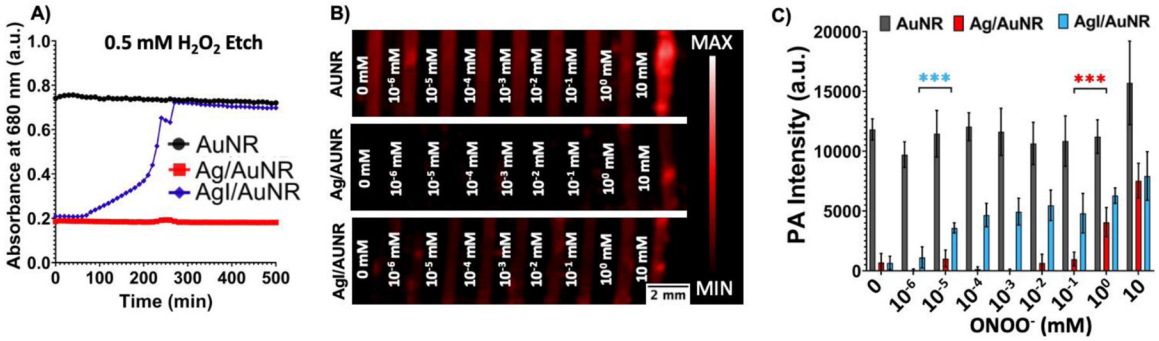

Figure 4. Etching kinetics and photoacoustic response.

With 0.5 mM H_2O_2, AgI/AuNR takes ~5 hours to completely etch whereas AuNR and Ag/AuNR show no change in absorbance for over 9 hours. **(A)** Photoacoustic images at 680 nm of AuNR, Ag/AuNR and AgI/AuNR treated with varying concentration of $ONOO^-$ (**B**). Plot comparing photoacoustic intensity of nanoparticles after treatment with varying concentrations of $ONOO^-$ from B (**C**). The detection limit for AgI/AuNR was 10^{-5} mM and for Ag/AuNR was 1 mM ($p < 0.001$). Error bars represent the standard deviation of six regions-of-interest.

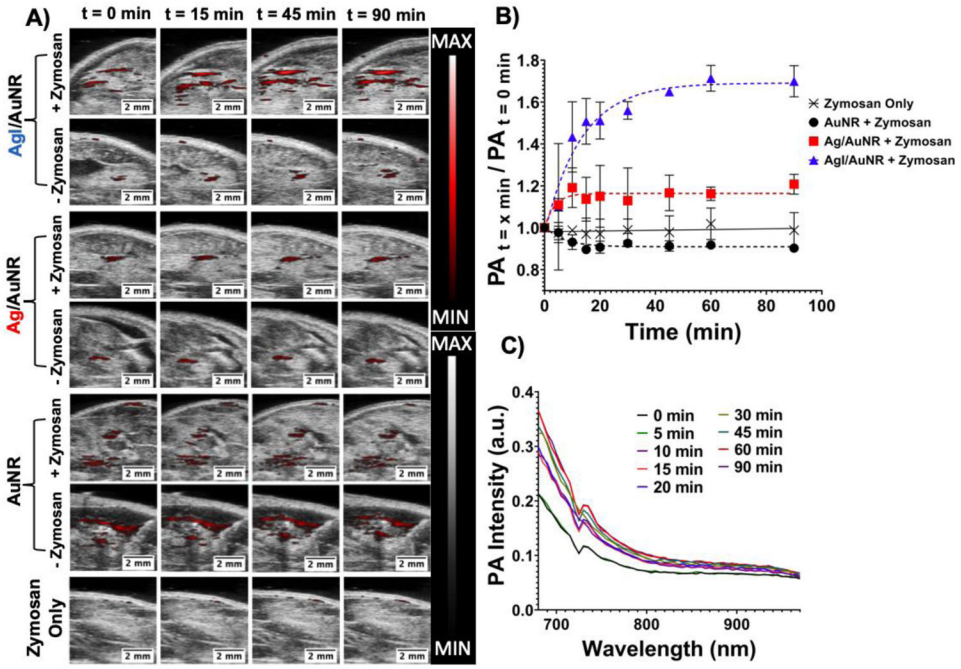

Figure 5. ***In vivo*** **photoacoustic oxidative stress sensing.**

Zymosan was used to generate oxidative stress intramuscularly in a murine model (*n = 3*). Photoacoustic images acquired at 680 nm. Signal was monitored at t = 0, 5, 10, 15, 20, 30, 45, 50, and 90 minutes. Representative photoacoustic-ultrasound images of AgI/AuNR, Ag/AuNR, and AuNR with and without zymosan treatment (**A**). Photoacoustic intensity at t = x min / photoacoustic intensity at t = 0 min for zymosan only and nanoparticles treated with zymosan (**B**). There is a 70% increase in photoacoustic signal for AgI/AuNR, 20% increase for Ag/AuNR, and 10% decrease for AuNR over 90 minutes. The zymosan-only control remains unchanged. Photoacoustic spectra of AgI/AuNR (+ zymosan) shows increasing photoacoustic response at 680 nm over 90 minutes (**C**). Error bars represent standard deviation of three replicate animals.